Precision Landing Performance of a Human-Scale Lunar Lander Using a Generalized Simulation Framework

Rafael A. Lugo,[1] Alicia Dwyer Cianciolo,[2] Soumyo Dutta,[3]
R. Anthony Williams,[4] and Justin S. Green[1]
NASA Langley Research Center, Hampton, Virginia, 23681, USA

Po-Ting Chen[5]
Jet Propulsion Laboratory, Pasadena, California, 91109, USA

Sarah D'Souza[6]
NASA Ames Research Laboratory, Moffett Field, California, 94035, USA

Alejandro R. Pensado[6]
Analytical Mechanics Associates, Hampton, Virginia, 23666, USA

NASA has established goals of returning humans to Moon with an initial landing by 2024 and a subsequent sustained presence by 2028, which will require technological advances in spacecraft navigation to enable precision landing. The ability to assess the navigation performance of these new and existing technologies is critical to identifying areas of risk reduction and investment. To that end, the Safe and Precise Landing Integrated Capabilities Evolution (SPLICE) project has demonstrated that a detailed six degree-of-freedom integrated performance simulation framework can provide information on and assessment of expected navigation performance. This framework incorporates engineering models of the on-board spacecraft guidance, navigation, and control systems at varying levels of fidelity. Recent advances in the development of this integrated performance simulation permit running these systems "in-the-loop," rather than assuming perfect knowledge of the spacecraft states. This development, coupled with fast simulation time and modularization of the various system models, enables a wide variety of system trades to be assessed at once. This paper presents a summary of the advances in the SPLICE simulation framework, updates to the spacecraft navigation models, and an application of the framework to characterize the precision landing performance of a human-scale lunar lander. A series of trade studies examining effects of ground state update qualities shows that given all other assumptions, sufficiently accurate Deep Space Network (DSN) measurements can enable safe and precise human-scale Lunar landings.

[1] Aerospace Engineer, Atmospheric Flight and Entry Systems Branch, AIAA Member.
[2] Aerospace Engineer, Atmospheric Flight and Entry Systems Branch, AIAA Associate Fellow.
[3] Aerospace Engineer, Atmospheric Flight and Entry Systems Branch, AIAA Senior Member.
[4] Research Computer Scientist, Atmospheric Flight and Entry Systems Branch.
[5] Member of Technical Staff, Guidance and Control Section.
[6] Aerospace Engineer, Atmospheric Flight and Entry Systems Branch, AIAA Member.

I. Introduction

Recent NASA studies of crewed missions to the Moon and Mars have highlighted the need for an autonomous safe and precise landing capability [1, 2]. The payload and mass requirements for these human-scale missions are orders of magnitude higher than previous robotic-scale missions. Numerous challenges must be addressed and technologies matured before these types of landings become feasible, including in the areas of spacecraft guidance, navigation, and control (GN&C).

The Safe and Precise Landing Integrated Capabilities Evolution (SPLICE) project is tasked with advancing autonomous spacecraft navigation through multiple areas of research and development. A crucial aspect of this effort is increasing the technology readiness level (TRL) of key deorbit, entry, descent, and landing (DDL/EDL) GN&C systems. Detailed six degree-of-freedom (6DOF) physics-based engineering simulations are used to aid in evaluation of these systems in an integrated performance sense [3]. Different navigation sensors and their effects on overall system performance are evaluated using these simulations.

In this work, an update to [3] is presented with application to the human-scale Lunar lander described in [4]. A brief description of the lander and concept of operations is provided in Section II. Updates to the models built to represent navigation sensors and other spacecraft systems are described in Section III. Finally, the results are presented in Section IV with emphasis on how improved modeling fidelity enables rapid and detailed assessment of the overall integrated system performance.

II. Human-Scale Lunar Landing

The Artemis program began in 2019 with a directive to return humans to the Moon by 2024 [5]. To that end, NASA awarded contracts in May 2020 to three companies to mature the design of an integrated Lunar lander vehicle [6]. Throughout this period, NASA maintained a government reference design for a Lunar lander that was continuously refined in parallel with the contractor efforts. The present analysis will focus on the government design.

A. Deorbit, Descent, and Landing Vehicle

Though the Artemis program relies on industry-provided lander designs, the vehicle used in the present study is from an abbreviated NASA Design Analysis Cycle (Mini-DAC) that focused a storable propellant system that does not rely on cryogenics, increasing the readiness of the design for 2024 [4]. The design is a two-element architecture with a Descent Element (DE) and Ascent Element (AE). Table 1 lists relevant vehicle information and assumptions.

Table 1 DDL vehicle information.

System	Parameter	Value
Mass	Mass	33,151 kg
	Main Engine Propellant Load	14,425 kg
Propulsion	Main Engines	3x 8000 lbf @ 340 s Isp
	RCS	16x 100 lbf @ 300 s Isp
Actuators	Main Engines	TVC, ±10°

B. Concept of Operations

The DDL concept of operations of the Mini-DAC design for the Artemis Lunar lander is shown in Fig. 1. DDL begins in the 100 km circular parking orbit. The deorbit insertion (DOI) burn places the vehicle in an intermediate 100x15.24 km orbit, and powered descent initiation (PDI) begins at periapsis with the braking burn performed by the DE. The braking burn is designed to reduce the vehicle velocity as efficiently as possible. The vehicle then transitions to the approach phase, during which the vehicle orientation is adjusted to use the landing navigation sensors. During this phase, vehicle thrust is controlled such that once the vehicle is over the landing site, horizontal velocity is nullified. Note that the “braking” and “approach” nomenclature is a holdover from the Apollo Moon landings. Terminal descent begins at an altitude of 50 m at 5 m/s, and the vehicle velocity is further reduced such that the main engines cut off at an altitude of 1 m and a velocity of 1 m/s.

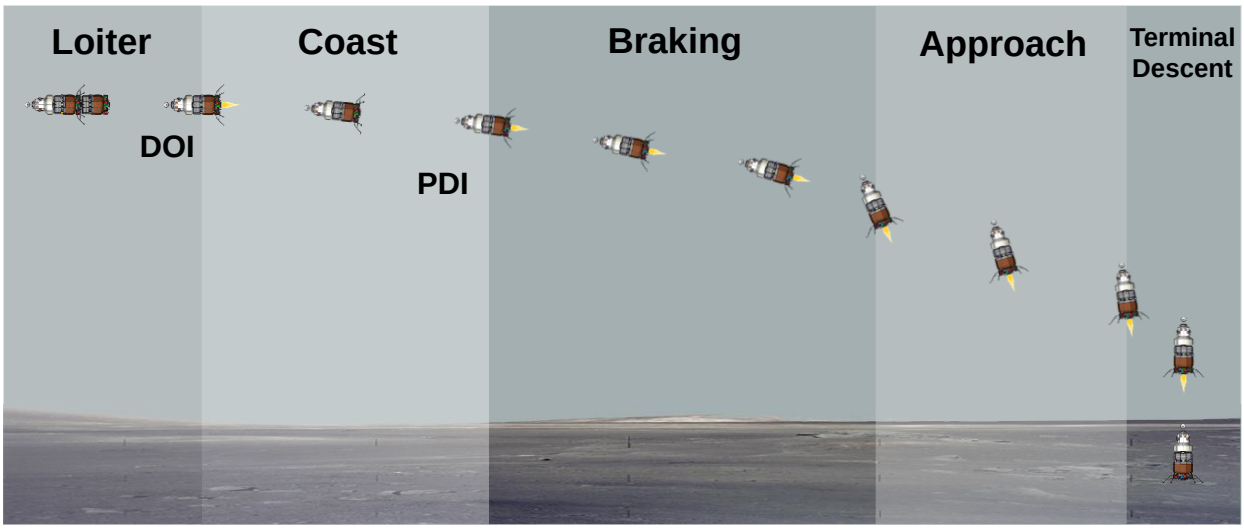

Fig. 1 Artemis Lunar lander DDL concept of operations, government reference design.

C. Navigation Sensor Ground Rules and Assumptions

Fig. 2 shows which navigation sensors are used in each mission phase. Dark gray bars indicate the sensor in that row is inactive. Inertial measurement unit (IMU) measurements are made continuously and throughout all phases of flight. Star tracker measurements cease at DOI, resume during the coast phase, and terminate 10 minutes prior to the start of the braking phase. A Deep Space Network (DSN) update is made five minutes prior to the deorbit burn. TRN measurements nominally begin during the braking phase and end prior to the approach and vertical descent phases, which are also referred to as terminal descent. Navigational Doppler LIDAR (NDL) measurements are made during the latter phases of powered flight, typically prior to terminal descent.

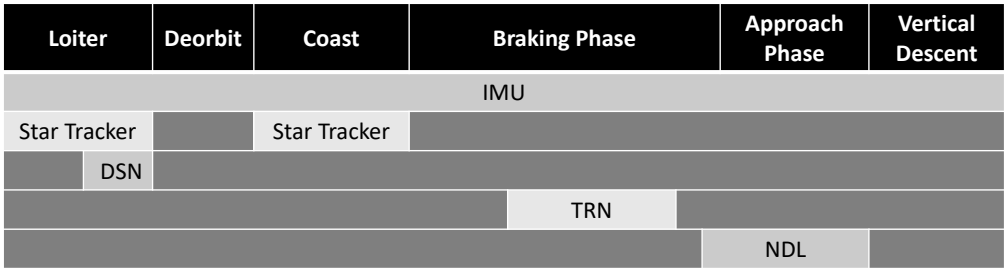

Fig. 2 Navigation sensor concepts of operation.

Various assumptions were made in the implementation and use of the navigation sensors for this work. As the simulation framework matures, these assumptions will be revised and updated:

- All sensors are mounted perfectly to the rigid body with known alignments (i.e., no sensor-to-body frame misalignments).
- The IMU is calibrated during an unmodeled on-orbit quiescent period, resulting in a reduction of the scale factor and biases by a factor of 10 for the remainder of the flight.
- IMU measurements below the thresholds listed in Table 2 are rejected by the navigation filter to avoid integrating noise. This measurement rejection occurs only during the loiter and coast phases.
- IMU measurements are not quantized.
- The navigation filter process noise includes IMU-related noise only.
- The DSN update is treated as a filter re-initialization rather than a measurement. This means that the DSN state measurement and associated covariance replaces the current filter state and covariance.
- Estimated vehicle mass properties (mass, inertias, and center of gravity location) are obtained directly from the simulation truth values.
- Lag time between sensor measurements and filter processing is unmodeled.

- Spacecraft clock time is the same as the simulation truth time.
- The target landing site (i.e., latitude, longitude, altitude) is known perfectly.

III. Simulation Framework and System Modeling

The DDL case study described in Section II is simulated using the Program to Optimize Simulated Trajectories II (POST2) 6DOF framework presented in [3]. This framework consists of generalized, modular, and user-configurable engineering models of various vehicle systems.

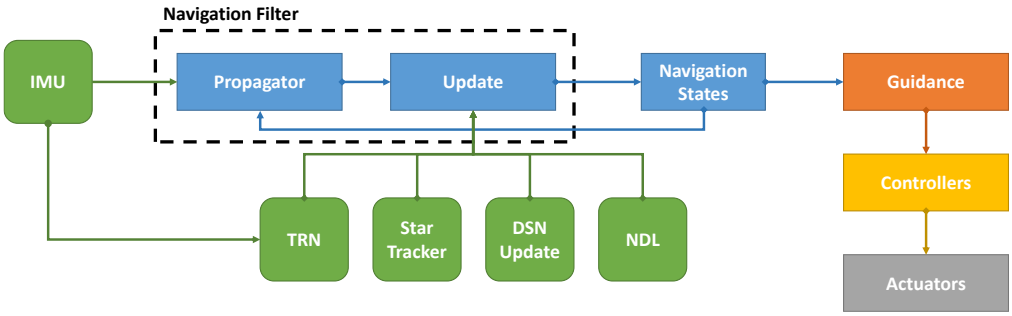

Fig. 3 GN&C block diagram.

The overall GN&C system architecture is illustrated as a block diagram in Fig. 3. The navigation system is shown as green and blue boxes. Sensor measurements are derived from simulation truth states. The outputs of the navigation system, in the form of vehicle states and associated derived quantities, are then passed to the guidance, which determines the necessary commands to achieve the desired final state. These commands are passed to the vehicle controllers, which then compute the necessary actuator states to achieve those commands. Finally, these states are passed to the vehicle actuators and propulsion systems, which impart forces and moments on the vehicle. This section describes the individual models that comprise the GN&C system in the integrated simulation. While some considerations for sensor accommodation on the reference government vehicle are made for each GN&C subsystem element, specific details of sensor accommodation and performance will be vehicle and mission dependent.

A. Guidance and Control

The G&C laws used during DDL are shown in Fig. 4. The Artemis lander uses the Apollo powered descent guidance based on formulations in [7]. During deorbit and coast phases, attitude control is provided by reaction control system (RCS) thrusters. A generalized three-axis phase-plane controller [8] directs RCS jet firings to minimize the errors between the commanded and navigated attitude and attitude rates.

	Loiter	Deorbit	Coast	Powered Descent	Vertical Descent
Propulsion	RCS			Main Engines & RCS	
Guidance	Open-Loop			Apollo PDG	Vertical
Steering Law	Attitude Hold			Polynomial Acceleration Profile	Vertical
Roll Control	RCS				
Pitch/Yaw Control	RCS			TVC	
Roll Control Law	Phase-Plane				
Pitch/Yaw Control Law	Phase-Plane			PID + Allocator	

Fig. 4 Guidance and control laws per major trajectory phase.

During powered descent, RCS is used for roll control only. Pitch and yaw control are provided by the three DE main engines. Pitch and yaw commands are passed through a proportional-integral-derivative (PID) controller to generate desired angular acceleration commands, which are then in turn passed through a thrust vector control (TVC) allocator to determine jet firings.

B. Navigation

The simulation framework includes a suite of spacecraft navigation models that are generalized to the extent that they can be used to simulate sensors of varying quality for a variety of mission scenarios. The full sensor suite is described in [3] and includes engineering and behavioral models of a strapdown IMU, star tracker, altimeter, velocimeter, navigational Doppler light detection and ranging (LIDAR, NDL), terrain-relative navigation (TRN), hazard detection (HD), and a ground update/Deep Space Network (DSN). This section will detail new or improved model capability since the publication of [3].

1. Model Fidelity and Sensor Quality

SPLICE has been supporting the development of various sensor models for use in performance assessments of various navigation scenarios. To this end, SPLICE has adopted a tiered approach to model fidelity and sensor quality so trade studies may be performed [3].

Model fidelity refers to the level of detail the model captures the underlying physical and mechanical processes of the sensor. For example, a low-fidelity IMU model may just be corrupted simulation truth states. A high-fidelity IMU model might capture the physical of the IMU sensing mechanism, voltage changes, etc. Note that higher fidelity does not necessarily indicate a "better" model, as the appropriate fidelity of the model depends on the application. Most of the models used in the present study are of low- or medium-fidelity and are designed to be able to capture a wide range of performance, or sensor quality.

Sensor quality refers to how accurately the sensor measurements reflect truth. The precise definition of high, medium, and low quality is subjective and depends on the type of sensor. For example, a low-quality IMU might be a commercial system intended for robotics hobbyists that has relatively large noise, scale factor, and bias attributes. A high-quality IMU might be a military-grade unit that has comparatively small noise, scale factor, and bias attributes.

2. Multi-Mode Extended Kalman Filter

An extended Kalman filter (EKF) provided by the NASA Engineering & Safety Center (NESC) was implemented in the simulation framework [9]. This multi-mode EKF (MEKF) is designed as an easily configurable navigation filter that can be used for various mission scenarios. The MEKF includes built-in navigation models for an IMU, star tracker, altimeter, and velocimeter. The MEKF has been augmented by adding similar models for TRN, NDL, and ground station updates. For the present study, the filter process noise only includes terms related to the IMU measurements.

3. Terrain-Relative Navigation

A medium-fidelity TRN model was implemented in the simulation. Having TRN measurements available during DDL/EDL is critical for precision landing capability. The TRN sensor provides lander position measurements relative to a planet-fixed coordinate system. The purpose of this sensor model is to capture the behavior of a passive camera-based TRN system, which extracts the surface coordinates of landmark features in the camera image by matching these features to a reference map. Using these matches, a Kalman-type filter or least squares estimator is used to estimate lander position.

The TRN sensor model in this simulation has a similar architecture, namely feature matching and state estimation. However, to limit the modeling scope, this model is behavioral and does not render images or perform image processing. Instead, it simulates uniformly distributed feature matches using the camera field-of-view and the true lander state. Each feature match is then corrupted by several error sources to mimic the image processing errors of a real system. These error sources include cross-correlation matching error, outlier error, map quantization error, and horizontal feature bias at both the local level and regional level.

For the estimation step, the sensor model leverages state space modeling because it provides a relatively straightforward method to relate TRN position accuracy to the basic system parameters like camera direction, field-of-view, image resolution, reference map resolution, etc. Parameter uncertainties like camera misalignment and focal length error are considered. The model has built-in internal checks that ensure the operating envelope of the TRN system is not violated. These checks include maximum and minimum altitudes, speeds, body rates, etc. The estimation algorithm in the model is based on the formulation presented in [10]. This approach has the same lineage as the fine matching mode of the Lander Vision System (LVS) on the Mars 2020 lander [11]. This similarity allows the position accuracy of the TRN sensor model to be tuned using 2019 LVS helicopter field test data. The TRN sensor model consists of an internal EKF in which attitude, velocity, and position states are initialized by the MEKF. The model can be used as a least squares estimator or as a parallel filter. Depending on the selection, the feature measurements refine either the prior MEKF estimate or an independent IMU estimate to produce a position measurement for the MEKF.

The standalone sensor model implementation is verified using Monte Carlo simulation. The ensemble error statistics match with the filter predicted error statistics. This indicates the output of the code implementation is consistent with the modeling assumptions.

An example plot for the position accuracy of the TRN sensor model is shown in Fig. 5. In this example, 2 different map resolutions are used over the altitude range of 6 km to 500 m. The map switching occurs at 25 s. When the 6.3 m/pixel reference map is used, the horizontal position accuracy is 22 m (3σ). When the 1.8 m/pixel map is used, the position accuracy improves to 7 m (3σ). It is important to note that the position accuracy remains relatively unchanged after the first update using a particular map. This behavior is a result of the regional feature bias error in the reference map.

For this analysis, the TRN camera is mounted near the vehicle CG and is angled at a 45° angle away from the vehicle centerline.

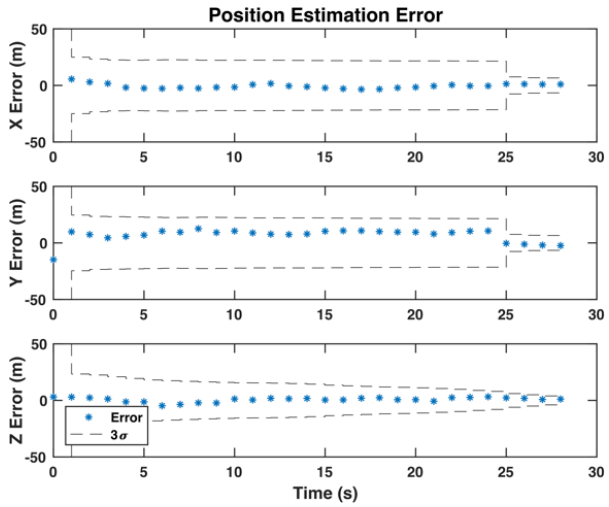

Fig. 5 Example position estimate error from the TRN sensor model.

4. Navigational Doppler LIDAR

Each NDL beam produces two fundamental measurements: range (distance along beam to terrain intercept) and the component of the planet-relative velocity vector projected onto the beam. The NDL measurement model utilizes the POST2 antenna subsystem model to simulate each of the three LIDAR beams. The beams are assumed to be rigidly fixed to the vehicle at a common mounting location, and the direction of the beams in the body frame are assumed to be known perfectly. The POST2 antenna subsystem calculates the range between the beam source and terrain intersection point [12]. For this work, the NDL mounting location (i.e., beam origin location) is at the base of the vehicle near the main engines. The beams are angled away from the centerline by 10° and beams B and C are separated from the center beam A by 120°.

An NDL measurement error model provided by the LaRC NDL team [13, 14] was also implemented in the simulation. The model ingests truth values produced by the measurement model and outputs corrupted measurements that are then passed to the MEKF. This error model applies errors as a function of modulation period and bandwidth, beam wavelength, frequency, and pointing knowledge. The measurement uncertainties are assumed to be 2.5 m 1σ in position and 0.015 m/s 1σ in velocity.

5. Sensor Performance Parameters

A summary of the sensor performance parameters is listed in Table 2 and are adapted from various sources. The star tracker and DSN models are of low fidelity, meaning they are simply corrupted truth values using the dispersions in Table 4. Only a subset of the NDL parameters are listed to the sensitive nature of some specific performance parameters.

Table 2 Sensor performance parameters.

Sensor	Parameter	Value
IMU [2]	Quality	High
	Measurement Frequency	200 Hz
	Measurement Threshold Variance	1e-5 m/s, 1e-6 rad
TRN [10]	Quality	High
	Measurement Frequency	1 Hz
	Operational Range	6.0-1.5 km altitude
	Field of View	90°
	Number of Maps	4
	Observable Features	100
	Feature Bias	1.1x map resolution
	Camera Pointing Knowledge Error	0.5° 3σ
	Feature Matching Failure	6.6%
	Camera Focal Length	0.006 m
	Minimum Map Resolution	1 m/pixel
	Pixels Per Axis	1024
NDL [13, 14]	Operational Range	3.0-0.03 km altitude
	Measurement Frequency	20 Hz
Star Tracker [2]	Quality	High
	Measurement Frequency	0.1 Hz

C. Monte Carlo Analysis

Varying key vehicle design parameters permits evaluation of the robustness of the integrated vehicle systems while providing an assessment of overall vehicle performance. Vehicle parameters varied for this study are listed in Table 3. Specific navigation sensor dispersions are listed in Table 4. Dispersions listed as single values apply to all three axes. DSN measurement uncertainties are provided in a velocity-relative u-v-w frame. Monte Carlo analyses consisting of 8,000 distinct trajectories (i.e., samples) were performed for each study outlined in the next section.

Table 3 Monte Carlo Dispersions. Dispersions listed as triplets refer to X/Y/Z axes unless otherwise noted.

Category	Parameter	Dispersion	Distribution
Initial Conditions	Body Rates	0.3°/s 3σ	normal
	Attitude (Velocity-relative)	3.0° 3σ	normal
	Uncorrelated state covariance	0.03º 3σ for angles, 0.03 km 3σ for altitudes	normal
Propulsion	Peak thrust	Scale factor: 1% 3σ	normal
	Isp	Scale factor: 1% 3σ	normal
Mass	Mass	250 kg 3σ	normal
	Center of gravity	0.05 / 0.01 / 0.01 m 3σ	normal
	Moments of inertia	1% kg-m^2 3σ	normal
	Products of inertia	1% kg-m^2 3σ	normal

Table 4 Navigation sensor dispersions. Dispersions listed as single values apply to all three axes. Dispersions listed as triplets refer to X/Y/Z axes unless otherwise noted.

Sensor	Parameter	Dispersion (X/Y/Z Axes)	Distribution
IMU	Accelerometer Misalignment	17 arcsec 3σ	normal
	Accelerometer Scale Factor	450 ppm 3σ	normal
	Accelerometer Bias	84 micro-g 3σ	normal
	Accelerometer Velocity Random Walk	0.003 m/s^2 3σ	normal
	Gyroscope Misalignment	19 arcsec 3σ	normal
	Gyroscope Scale Factor	27 ppm 3σ	normal
	Gyroscope Bias	0.036 °/hr 3σ	normal
	Gyroscope Angular Random Walk	0.015 °/√hr 3σ	normal
Star Tracker	Bias	8 arcsec 3σ	normal
	Boresight Noise	24 arcsec 3σ	normal
DSN Update	Position Bias (u-v-w frame)	500 / 1000 / 200 m 3σ	normal
	Velocity Bias (u-v-w frame)	0.05 / 0.10 / 0.01 m/s 3σ	normal
NDL	NDL Error Model		
Optical TRN	See TRN sensor specifications in Table 2		

1. Definitions

The present work uses the following definitions regarding navigation errors. Consider a simulation analysis of a spacecraft attempting to reach a target. The dispersion of truth states $\boldsymbol{x}$ is the collection of the true spacecraft states at a given time or event such as touchdown. The dispersion of navigation states $\hat{\boldsymbol{x}}$ is the collection of the estimated spacecraft states as computed by the onboard navigation filter at that corresponding time or event. In the present work, the navigation error is defined to be the difference between the true state and the navigation state, computed as the root-sum-squared (RSS) of the difference between the truth and navigation state vectors. These parameters are illustrated in Fig. 6.

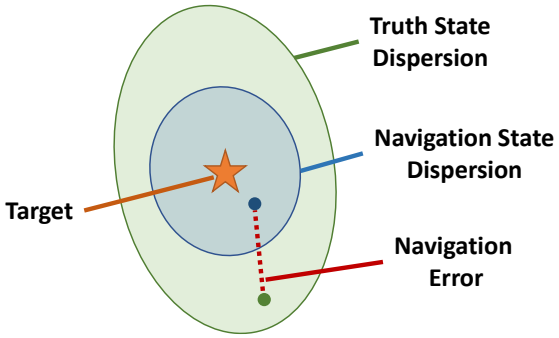

Fig. 6 Dispersion and error definition.

2. Performance Metrics

While the integrated performance simulation framework permits the assessment of a wide variety performance parameters, the present study will focus on those related to navigation:

1. *Navigation error:* This parameter, while not a single value, describes the overall behavior of the navigation system. Specifically, the navigation errors at specific events are assessed to understand how the various navigation sensors, when activated and deactivated, affect the evolution of the navigation error.
2. *Landing precision:* This parameter describes how well the integrated vehicle lands near the pre-designated target. Currently, a landing precision (i.e., range to target at touchdown) of 100 m in a 3σ sense is desired. For this analysis, it is assumed that the inertial location of the landing site is known perfectly (e.g., is not dispersed), and that the same location is used for GN&C targeting. The present study will also assess landing precision in a 99%-tile sense to better capture the effects of outliers.
3. *Success rate:* The success rate describes the percentage of 8,000 Monte Carlo samples that achieve a safe (or successful) landing. The present study defines a safe landing as one that reaches the touchdown event with a

horizontal (translational) velocity of less than or equal to 1.0 m/s, a vertical velocity of less than 3.0 m/s, an angle off of vertical of less than 3°, and a maximum angular rate about any axis of less than 0.5°/s. A success rate of 99% or better is desired.

Note that the success rate as defined here does not capture a precise landing, since that is captured by the previous performance metric. This means that any given Monte Carlo sample can land precisely but not safely, and vice versa.

3. Filter Consistency

Performance of the navigation filter can also be evaluated using a normalized error square (NES) filter consistency test [15]. A filter that is consistent means the state estimate uncertainties defined by the filter covariance accurately represent the actual navigation state dispersions. The NES is defined as $N_k^2 = (\boldsymbol{x} - \hat{\boldsymbol{x}}_k)^T \hat{P}_k^{-1} (\boldsymbol{x} - \hat{\boldsymbol{x}}_k)$ where $\boldsymbol{x}$ is the true state vector, $\hat{\boldsymbol{x}}$ is the estimated state vector, $\hat{P}$ is the filter state covariance, and k is the time index. The NES is computed for each Monte Carlo sample then averaged across all Monte Carlo samples. The filter is consistent if this parameter satisfies $N_k^2 \in \left[\chi^2_{n,p} \quad \chi^2_{n,1-p}\right]$ where χ^2 is the chi-squared probability distribution, n is the number of observations or degrees of freedom, and p and $1-p$ define the bounds of the desired significance level. In the present analysis, only the states (position and velocity) will be considered so that there are a total of six observations, and the desired significance level is chosen to be 5% (e.g., the two-sided 95% interval). Thus, the filter is consistent if $N_k^2 \in [5.924 \quad 6.076]$.

IV. Results

Results from the POST2 simulations of the government reference Artemis lander at the Moon with navigation running in-the-loop are presented in this section. To demonstrate the ability to perform trade studies, several Monte Carlo analyses were run with varying DSN measurement qualities. Recall from Section II.C that the DSN updates are treated as filter reinitializations. The results use the following labels:

1. SPLICE: High quality DSN measurement (baseline SPLICE specifications). Uses the position and velocity dispersions from Table 4.
2. DSN 50%: High quality DSN measurement with position and velocity bias dispersions reduced by 50%. Represents a more accurate state update such as that obtained with more on-orbit tracking, additional tracking stations, etc.
3. DSN 10%: High quality DSN measurement with position and velocity bias dispersions reduced by 90%. Represents near-perfect state knowledge.
4. DSN Pos 10: High quality DSN measurement with position bias dispersions reduced by 90%. Chosen to study sensitivity to position vs. velocity uncertainty.

These trades were selected to illustrate the sensitivity of navigation performance to the DSN update. In general, DSN measurement uncertainties can be improved by tracking the vehicle across longer orbital arcs or using more ground tracking stations. These methods depend on the specific orbital parameters and how long the vehicle is in view of the various Earth ground stations, so these cases can be considered a simplified trade study.

Fig. 7 shows the landing precision metric (actual range to target at touchdown) results for all trades. Histograms are shown at top-left, gaussian quantiles that illustrate how well the dispersions follow a normal distribution are shown at top-right, and statistics are shown at the bottom. The quantile plot emphasizes that for certain parameters, considering only standard deviations (σ) can be misleading since the typical standard deviation assumes a gaussian distribution. As the distributions deviate from gaussian (shown by the dotted solid line on the quantile plot), the standard deviation becomes less representative of the underlying data. For this reason, other statistics are computed and shown. In particular, the 99%-tile is used by the authors to evaluate performance, as it better captures the behavior of the tails of the distribution.

From these results, it is seen that the SPLICE-provided DSN update leads to a markedly poor success rate (80.2%). Of those successful cases, however, the landing precision (36.4 m 3σ, 45.84 m 99%-tile) is within the 100 m requirement. Note here how the standard deviation is significantly lower than the percentile. Thus, running with the SPLICE high quality DSN update permits precise but not safe landing. This also indicates that a lower quality DSN measurement is unlikely to provide the performance required by the Artemis lander.

When the DSN update noise dispersions are reduced to 50% of the original values (see DSN 50% column), there is improvement in both the success rate (97.0%) and landing precision (42.13 m 99%-tile), which could satisfy the requirements since a minimum success rate requirement has not been explicitly defined. When the DSN update noise

dispersion is reduced to 10% of the original value, diminishing returns are observed in both the success rate (greater than 99%) and landing precision (41.42 m 99%-tile). The fourth trade, in which the position noise dispersions are reduced to 10% of the original values but the velocity dispersions are left at the original high quality SPLICE specification, has the success rate (greater than 99%) and landing precision (41.61 m 99%-tile) remain essentially unchanged. Thus, most of the performance improvement can be obtained through improving the vehicle position uncertainty, though the specific degree of tracking accuracy improvement is dependent on number of available and visible ground stations, time spent continuously tracking, etc.

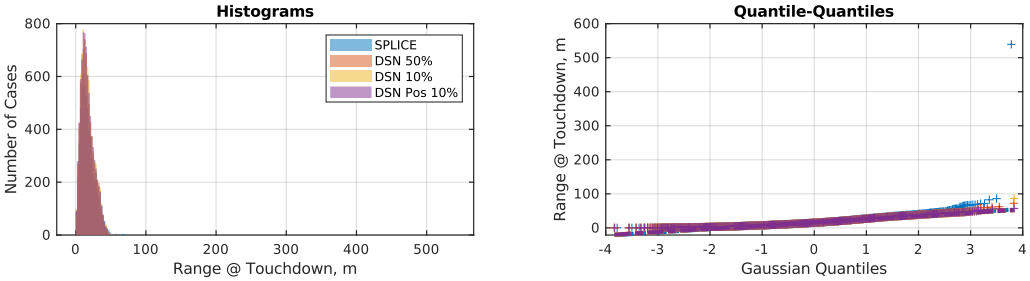

	SPLICE	DSN 50%	DSN 10%	DSN Pos 10%
Nominal	16.66	18.46	13.13	12.67
Mean	17.32	16.8	16.93	16.85
3-sigma	36.4	28.26	28.02	28.03
1.00 %-tile	1.66	1.84	2.09	1.88
99.00 %-tile	45.84	42.13	41.42	41.61
Max Value	539.19	72.25	86.61	57.24
Min Value	0.23	0.22	0.11	0.17
Success	6412	7756	7997	7995
Percent	80.2	97	100	99.9

Fig. 7 Touchdown precision statistics. A success rate of 100% is listed for the DSN 10% case due to rounding.

To provide some context to these dispersions, Fig. 8 shows how the vehicle position dispersions evolve over time in a downrange-crossrange-altitude space relative to the landing target for the DSN 10% trade. The data shown focus on the latter part of powered descent, from TRN activation to touchdown. These views emphasize how far away from the target the TRN and NDL sensors are active, and how the trajectory dispersions are reduced as the sensors work to "clean up" navigation errors. An example of this is shown by the altitude spread at the "TRN On" (cyan dots) and "NDL On" (purple dots) events, both of which are triggered by the navigated altitude estimate rather than a truth altitude. By the time the NDL is activated at a 3 km altitude, the spread in the points has essentially disappeared. This also emphasizes how critical navigation sensor measurements are to minimizing errors.

The red dots in Fig. 8 correspond to the five failed Monte Carlo samples in this trade. While they are generally clustered at lower altitudes at TRN activation, it is likely that these cases fail due to a combination of low altitude and either excessive or insufficient velocity, as well as attitude considerations, that would contribute to insufficient control authority.

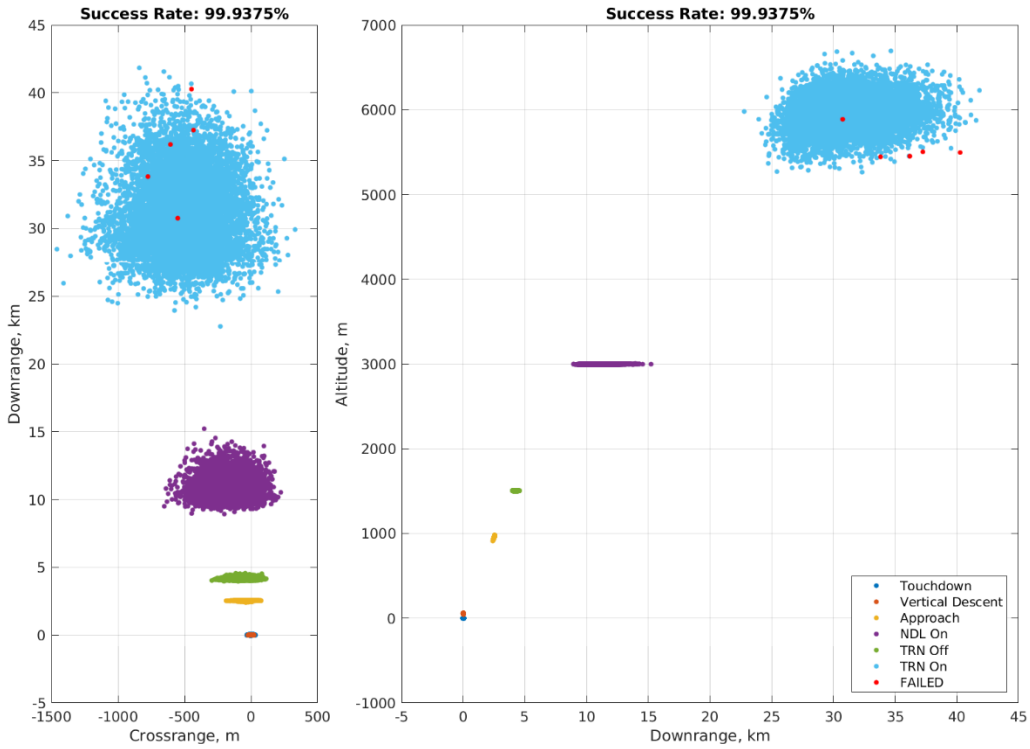

Fig. 8 Position dispersions, powered descent events, DSN 10% trade.

Fig. 7 shows the landing precision metric but does not provide information on navigation performance. Fig. 10 shows the navigated position error at PDI for each trade. Recall from Fig. 6 that navigation position error is the RMS of the difference between the truth and navigated position vectors. This event is useful because it illustrates how much error must be accommodated by the G&C systems at the start of powered descent. For example, when considering only this position space, the 99%-tile position error of 4218 m for the SPLICE case is too large for the G&C to correct, resulting in a low success rate. The 1393 m error for DSN Pos 10% case, however, is within the G&C control authority.

Fig. 10 shows the results of the navigated position error at touchdown for each trade. When considering trades two through four (improved DSN update quality), the consistent navigation position error of approximately 15 m 99%-tile shows how well the TRN and NDL sensors can "clean up" the errors during coast and early powered descent phases.

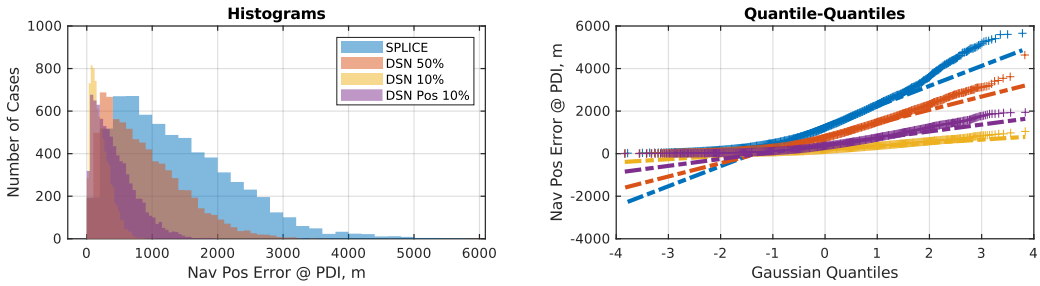

	SPLICE	DSN 50%	DSN 10%	DSN Pos 10%
Nominal	3111.59	1527.26	260.26	710.08
Mean	1387.74	866.72	214.28	433.05
3-sigma	2742.06	1788.27	449.66	961.98
1.00 %-tile	123.72	68.77	16.76	23.84
99.00 %-tile	4217.77	2622.58	656.94	1392.9
Max Value	5657.97	4636.55	1043.68	1942.55
Min Value	24.35	12.77	2.91	3.53
Success	6412	7756	7997	7995
Percent	80.2	97	100	99.9

Fig. 9 Position navigation error at PDI.

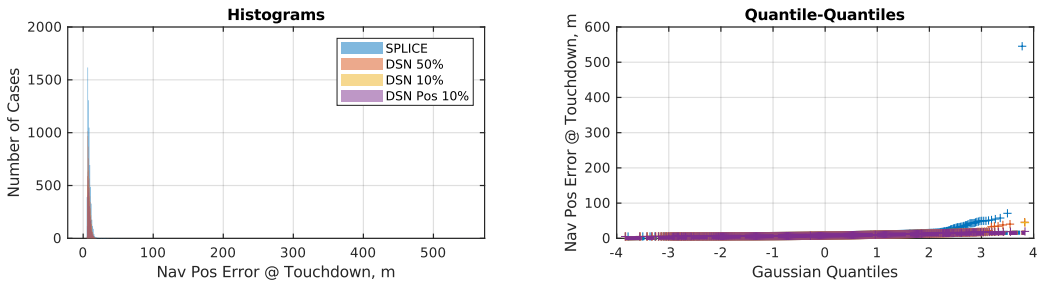

	SPLICE	DSN 50%	DSN 10%	DSN Pos 10%
Nominal	6.18	8.07	7.02	7.66
Mean	8.76	8.37	8.31	8.33
3-sigma	22.76	6.8	6.35	6.25
1.00 %-tile	5.66	5.67	5.65	5.64
99.00 %-tile	20.35	14.99	14.99	14.93
Max Value	545.38	45.95	44.5	19.7
Min Value	5.25	5.25	5.17	5.22
Success	6412	7756	7997	7995
Percent	80.2	97	100	99.9

Fig. 10 Position navigation error at touchdown.

Fig. 11 shows the precision landing performance at start of vertical descent and at touchdown in terms of crossrange and downrange for the fourth trade (DSN Pos 10%). This case provides adequate position performance for landing and indicates a possible change to the baseline DSN assumptions for future Artemis studies.

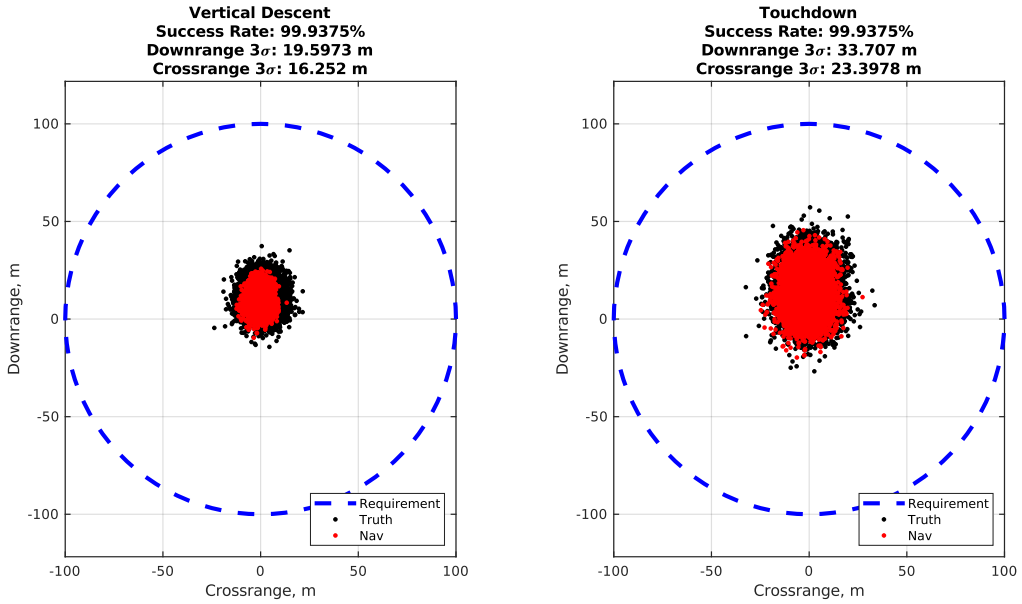

Fig. 11 Vertical descent and touchdown precision landing footprints, Trade 4, "DSN Pos 10%".

A summary of the relevant navigation performance results at various key events during the trajectory are listed in Table 5. Navigated position, velocity, and attitude errors are listed at DOI, PDI, and touchdown. Errors when the TRN is activated (TRN On), deactivated (TRN Off), and at the start of vertical descent are included to illustrate how the errors evolve throughout the trajectory. The accuracy of the DSN update, five minutes prior to DOI, is evident from the errors at DOI. There is a significant increase in the errors between DOI and TRN on, during which there are only star tracker updates during coast and IMU measurements. The TRN sensor significantly reduces the navigation errors, and NDL maintains low errors.

Table 5 Navigation error evolution across trajectories.

	SPLICE			DSN 50%			DSN 10%			DSN Pos 10%		
	Pos (m)	Vel (m/s)	Att (deg)	Pos (m)	Vel (m/s)	Att (deg)	Pos (m)	Vel (m/s)	Att (deg)	Pos (m)	Vel (m/s)	Att (deg)
DOI	819	0.24	0.004	418	0.13	0.004	87	0.03	0.004	92	0.09	0.004
PDI	4218	3.69	0.003	2623	2.23	0.003	657	0.58	0.003	1393	1.21	0.003
TRN On	4638	4.10	0.006	2818	2.53	0.006	728	0.71	0.006	1584	1.42	0.006
TRN Off	8	0.15	0.068	8	0.14	0.067	8	0.14	0.067	8	0.14	0.067
Vertical Descent	18	0.07	0.296	15	0.03	0.071	15	0.03	0.068	15	0.03	0.069
Touchdown	20	0.20	0.295	15	0.16	0.065	15	0.15	0.064	15	0.15	0.064

The NES filter consistency check was performed for a randomly selected dispersed trajectory and is shown in Fig. 12. The NES indicates that overall, the filter is not consistent and tends to either over- or underestimate the actual navigation dispersion since the NES exceeds the bounds specified by the 95% significance interval, plotted as dashed lines. There are two bounds to capture the maximum and minimum ranges of consistency, but are close together at this scale so they appear as a single line. While this study demonstrates the capability and utility of the simulation tool, a more rigorous filter tuning approach is required to improve the NES statistic and make the filter consistent across the entire trajectory. For example, adjusting the filter process noise to include dynamics modeling errors such as those due to onboard gravity model differences from truth would improve filter consistency.

The NES was also calculated for all Monte Carlo samples at touchdown and averaged across successful cases as described in Section III.C.3. For the fourth trade, the NES value was 95.420, beyond the range that represents a consistent filter (6.076), further illustrating that additional filter tuning is required.

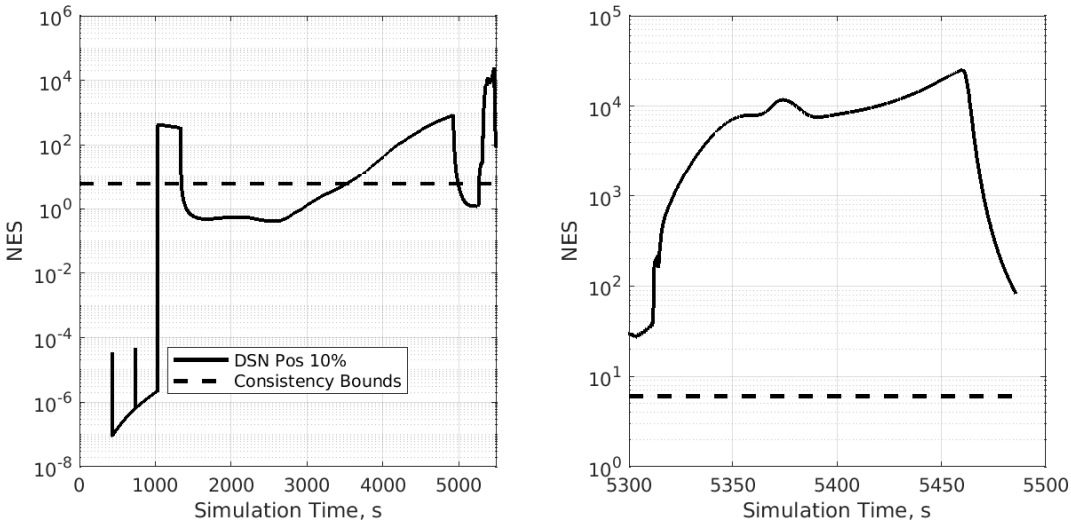

Fig. 12 NES filter consistency, dispersed Monte Carlo sample.

Finally, simulation runtime is an important metric when performing Monte Carlo analysis on many trade studies. The runtimes for the various Monte Carlos are listed in Table 6. The runtime is defined as the time elapsed from the start of first trajectory to the end of the final trajectory. Each Monte Carlo consists of 8,000 trajectories run on the Atmospheric Flight and Entry Systems Branch (AFESB) compute clusters at NASA Langley Research Center. A 1,000-node queue was used such that approximately 1,000 trajectories could be run simultaneously. Though there are only four samples here, on average the runtime was approximately ten minutes per trade study. This runtime is sufficiently short to enable a fast assessment of navigation performance using a full 6DOF simulation with integrated GN&C, from deorbit to touchdown.

Table 6 Monte Carlo run times.

Trade Study	Runtime
SPLICE	660 s (11.0 min)
DSN 50%	595 s (9.9 min)
DSN 10%	554 s (9.2 min)
DSN Pos 10%	578 s (9.6 min)

V. Summary and Conclusions

An extensive update to the generalized simulation framework presented in [3] has been presented. Various navigation sensor engineering models have been improved and added to enable rapid investigation of a variety of vehicles and missions in an integrated performance sense. An application of this framework to a human-scale Lunar lander was presented to emphasize the types of fast navigation analyses that can be performed using this generalized simulation framework.

The study of the human-scale Lunar lander showed that overall navigation performance given the design and analysis GR&As and a sufficiently accurate DSN measurements was satisfactory. In particular, better position accuracy can provide significant improvements in success rate. However, a filter consistency check revealed that the navigation filter was underestimating the actual navigation state dispersions, highlighting the need for additional filter tuning. It was also clear that it is insufficient to consider only a single performance metric as an indicator of vehicle robustness or mission success since the SPLICE baseline DSN accuracy specification resulted in the vehicle landing precisely but not safely in a statistical sense. Thus, careful consideration and selection of the specific performance metric must be accounted for when designing program requirements.

Additional future work will include trading TRN sensor performance with DSN accuracy to determine if increasing the altitude of the first TRN measurement may eliminate the need for the more precise DSN updates investigated in the study. Additionally, refining the sensor error models to include mounting misalignments will be necessary to capture more realistic dispersions.

Acknowledgments

The authors thank Eric Queen (LaRC) for RCS phase plane controller design, Chris Karlgaard (AMA) for supporting the implementation and testing of the MEKF in the simulation framework, and Diego Pierreottet (LaRC) for the NDL sensor error model. The authors are also grateful to Scott Striepe (LaRC), David Woffinden (JSC), George Chen (JPL), Ron Sostaric (JSC), and the HLS GN&C Discipline Team for helpful insight and discussions regarding this work. A portion of this research was carried out at the Jet Propulsion Laboratory, California Institute of Technology, under a contract with the National Aeronautics and Space Administration.

References

[1] Cianciolo, A.D., Striepe, S., Carson, J., Sostaric, R., Woffinden, D., Karlgaard, C., Lugo, R., Powell, R., and Tynis, J., "Defining Navigation Requirements for Future Precision Lander Missions," AIAA 2019-0661.

[2] Cianciolo, A. D., Korzun, A., Edquist, K., Samareh, J., Sostaric, R., Calderon, D., and Garcia, J. A., "Human Mars Entry, Descent, and Landing Architecture Study Phase 3 Summary," AIAA 2020-1509.

[3] Cianciolo, A. D., Dutta, S., Lugo, R. A., Williams, R. A., and Chen, P., "A Simulation Framework for Precision Landing and Hazard Avoidance Technology Assessments," AIAA 2020-0366.

[4] Craig, A. S., Anzalone, E. J., Hannan, M. R. , Belanger, B. L., Burke, L. M., Condon, G. L., Joyce, R. T., Mahajan, B., Summers, A. W., Means, L. L., and Pei, J., "Human Landing System Storable Propellant Architecture: Mission Design, Guidance, Navigation, and Control," AAS 20-592.

[5] Dunbar, B., "What is Artemis?" [website], URL: https://www.nasa.gov/what-is-artemis [retrieved 22 May 2020].

[6] Potter, S., "NASA Names Companies to Develop Human Landers for Artemis Moon Missions," [online article], URL: https://www.nasa.gov/press-release/nasa-names-companies-to-develop-human-landers-for-artemis-moon-missions [retrieved 22 May 2020].

[7] Sostaric, R. R., and Rea, J. R., "Powered Descent Guidance Methods for the Moon and Mars," AIAA 2005-6287.

[8] Calhoun, P. C., and Queen, E. M., "Entry Vehicle Control System Design for the Mars Smart Lander," AIAA 2002-4504.

[9] Murri, D. G., Striepe, S. A., and Powell, R. W., "NESC Report Assessment #09-00530, Phase 2: Simulation Framework for Rapid Entry, Descent, and Landing (EDL) Analysis," NESC-RP-09-00530. NASA-TM-2011-217063.

[10] Mourikis, A. I., Trawny, N., Roumeliotis, S. I., Johnson, A. E., Ansar, A., and Matthies, L., "Vision-Aided Inertial Navigation for Spacecraft Entry, Descent, and Landing," IEEE Transactions on Robotics, vol. 25, no. 2, pp. 264-280, 2009.

[11] Johnson, A., Aaron, S., Chang, J., Cheng, Y., Montgomery, J., Mohan, M., Schroeder, S., Tweddle, B., Trawny, N., and Zheng, J., “The Lander Vision System for Mars 2020 Entry Descent and Landing,” Proceedings of the Advances in the Astronautical Science Guidance Navigation and Control, vol. 159, no. 36, 2017

[12] Shidner, J., “An Efficient Ray-Tracing Method for Determining Terrain Intercepts in EDL Simulations,” 2016 IEEE Aerospace Conference, 2016, pp. 1-9, doi: 10.1109/AERO.2016.7500591.

[13] Gragossian, A., Pierrottet, D., Estes, J., Barnes, B. W., Amzajerdian, F., and Hines, G. D., “Navigation Doppler Lidar Performance at High Speed and Long Range,” AIAA 2020-0369.

[14] Pierrottet, D. F., Hines, G. D., Barnes, B. W., Amzajerdian, F., Petway, L. B., Carson III, J. M. , “Navigation Doppler Lidar Integrated Testing Aboard Autonomous Rocket Powered Vehicles,” AIAA 2018-0614.

[15] Crassidis, J. L., and Junkins, J. L., "Optimal Estimation of Dynamic Systems," Chapman & Hall/CRC, Washington, D.C., 2004.